

Small is beautiful, and dry[†]

ZHENG QuanShui^{1,2*}, LV CunJing¹, HAO PengFei¹ & SHERIDAN John²

¹Department of Engineering Mechanics, Tsinghua University, Beijing 100084, China;

²Department of Mechanical and Aerospace Engineering, Monash University, VIC 3800, Australia

Received June 25, 2010, accepted July 1, 2010

Thousands of plant and animal species have been observed to have superhydrophobic surfaces that lead to various novel behaviors. These observations have inspired attempts to create artificial superhydrophobic surfaces, given that such surfaces have multitudinous applications. Superhydrophobicity is an enhanced effect of surface roughness and there are known relationships that correlate surface roughness and superhydrophobicity, based on the underlying physics. However, while these examples demonstrate the level of roughness they tell us little about the independence of this effect in terms of its scale. Thus, they are not capable of explaining why such naturally occurring surfaces commonly have micron-submicron sizes. Here we report on the discovery of a new relation, its physical basis and its experimental verification. The results reveal that scaling-down roughness into the micro-submicron range is a unique and elegant strategy to not only achieve superhydrophobicity but also to increase its stability against environmental disturbances. This new relation takes into account the previously overlooked but key fact that the accumulated line energy arising from the numerous solid-water-air intersections that can be distributed over the apparent contact area, when air packets are trapped at small scales on the surface, can dramatically increase as the roughness scale shrinks. This term can in fact become the dominant contributor to the surface energy and so becomes crucial for accomplishing superhydrophobicity. These findings guide fabrication of stable super water-repellant surfaces.

scale effect, line tension, wetting, contact angle, superhydrophobic

PACS: 47.55.np, 47.55.dr, 68.08.Bc, 68.03.Cd, 87.15.La

Wetting on a rough substrate is considered to be either in the Wenzel [1] or Cassie-Baxter state [2]. In the former, the liquid follows the surface corrugations, as shown in Figure 1(a); in the latter the water drop is attached to the surface but in a position on top of the corrugations, which allows air pockets to be trapped under it, as shown in Figure 1(b). Usually, only one of these states is stable while the other is metastable [3–5], depending on both the surface chemistry and roughness. It is well known that wetting in the Cassie-Baxter, rather than Wenzel, state is energetically favorable if the hydrophobic surface is sufficiently rough [3–6] and this is generally considered to be a requirement for achieving superhydrophobicity [7]. In both states, mini-

mizing the system free energy can yield apparent contact angles, θ^* , that are functions of the intrinsic or chemical contact angle θ (measured on flat solids) and the topography of the roughness structure. Chemically modifying the surface alone can typically lead to intrinsic contact angles of up to 120° , but not more [8,9]. The relation between the apparent and intrinsic contact angles in the Wenzel state is given by $\cos\theta^* = r\cos\theta$. The parameter r is the ratio of the wet surface area to its projection or apparent area. In the Cassie-Baxter state, the classical form of the relationship is given by $\cos\theta^* = -1 + (1+\cos\theta)f$, where f is the area fraction of the wet part of the solid. The Wenzel and Cassie-Baxter relations, apart from some generalizations (concerning, for example, line-tension effects on nanometer-sized drops or more complex roughness topography), have classically been used to characterize the apparent contact angles with

*Corresponding author (email: zhengqs@tsinghua.edu.cn)

†Recommended by HONG YouShi

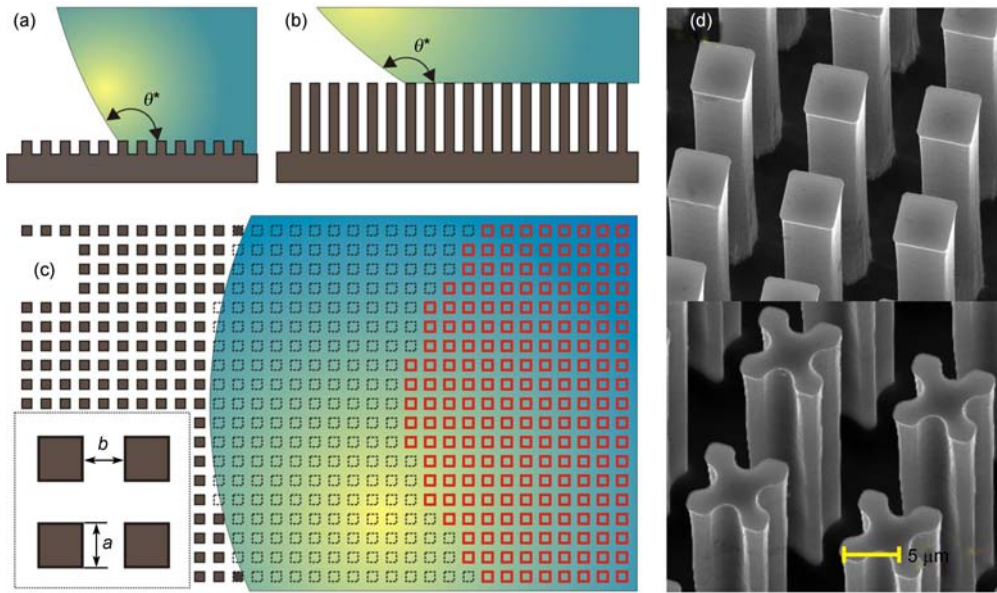


Figure 1 Wetting on pillar-structured surfaces: (a) Wenzel state, (b) Cassie-Baxter state, (c) the top view of the Cassie-Baxter state with numerous triple-phase lines (red) distributed over the apparent solid-water contact area, and (d) typical scanning electron microscope images of lithographic fabricated pillar-surface samples with square- and X-shaped pillar cross-sections.

remarkable success [10]. They also tell us that θ^* approaches 180° as the area fraction f decreases or, equivalently, the roughness ratio r increases. Recently, however, a number of exceptions have been observed that seem to be at odds with this understanding. For instance, in some very significant experiments [11–13], topographical shapes and sizes of roughness were shown to have a remarkable influence on advancing and receding contact angles. Debate on the physical basis of these results has been active but is unresolved to date.

In the Cassie-Baxter state, there can clearly be numerous triple-phase (solid-liquid-gas) intersection lines that coexist with the trapped air pockets, as schematically illustrated by the red lines in Figure 1(c). It is somewhat surprising that all known contact angle relations overlook the key fact that the total length, L_T , of the triple-phase intersection lines per unit of apparent contact surface area can become extremely large as the roughness scale shrinks into the micron-submicron range. Here we seek to include this effect in a new relationship for wetting applicable to surfaces with micron-submicron scale features. To formulate a precise relationship, we require a set of rough surfaces that can both be well-characterized and varied in the parameters that affect the contact angle. To obtain this, without losing the physical basis of the formulation, we consider the periodic pillar-structured surfaces shown in Figure 1. Using such surfaces, one can immediately characterize the triple-phase line length as $L_T = fS^{-1}$, where f is the area fraction and $S = A/L$ is a shape-dependent roughness scale, given by the boundary length L and area A of the pillar cross-sections. For the studied square and X-shaped cross-sections as illustrated in Figure 1,

S is equal to $a/4$ and $a/8$ respectively, where a is the side length of either shape. One can get even smaller S by using more complicated or even multiconnected shapes. For a square pillar structure with pillar side length $a = 1 \mu\text{m}$ and the pillar to pillar spacing $b = 1 \mu\text{m}$, the total triple-phase line length L_T per unit square meter is, amazingly, 1000 km! This result illustrates the potential for the accumulated total line energy $L_T\lambda$ to become significant as the roughness scale shrinks into the micron-submicron range, given that for various triple-phase combinations, the measured triple-phase line tensions λ are typically on the orders of magnitude $10^{-9} - 10^{-6} \text{ N}$ [14].

Attaching water to the pillar-structured substrate will change the system free energy per unit apparent area from $\sigma + f\gamma_{\text{sg}}$ to $(1-f)\sigma + f\gamma_{\text{sl}} + fS^{-1}\lambda$, where σ ($\sim 0.073 \text{ N/m}$) is the water surface tension, and γ_{sg} and γ_{sl} are the solid-gas (air) and solid-liquid (water) interfacial energies. Thus, the energy (E) released by this process of attachment is equal to $E = (1 + \cos\theta)(1 - l_{\text{cr}}S^{-1})f\sigma$, where the Young's relation $\cos\theta = (\gamma_{\text{sg}} - \gamma_{\text{sl}})/\sigma$ has been used, and

$$l_{\text{cr}} = \frac{\lambda}{(1 + \cos\theta)\sigma} = \frac{\lambda}{\sigma + \gamma_{\text{sg}} - \gamma_{\text{sl}}} \quad (1)$$

is an intrinsic or chemical length. Through a similar derivation to that for the Cassie-Baxter relation, one obtains

$$\cos\theta^* = -1 + (1 + \cos\theta) \left(1 - \frac{l_{\text{cr}}}{S}\right) f. \quad (2)$$

Compared with the Cassie-Baxter relation, (2) weights the

term that modifies the intrinsic contact angle by a new factor $(1 - l_{cr}/S)$, which plays a similar role to the area fraction f in determining the apparent contact angle. It is apparent that this factor becomes increasingly important as we scale down the surface roughness. This new result and its underlying mechanism provide significant new insights into how to achieve superhydrophobicity by shrinking the roughness scale (S).

To validate these findings, we first fabricated three sets of pillar-structured surface samples of size 1 cm×1 cm on a silicon wafer using photolithography (see Figures 1(c) and (d), or Appendix). Samples in Sets I and II are square-shaped with fixed $f \approx 0.15$ and 0.24 , respectively, and those in Set III are X-shaped with fixed $f \approx 0.24$. In contrast to f being constant, the pillar sizes S were designed to be variable. All had their surfaces become hydrophobic by grafting a self-assembled monolayer of octadecyltrichlorosilane (OTS, $C_{18}H_{37}Cl_3Si$, 95%) onto the samples. We used de-ionized water as the liquid, formed into droplets of 10 μ L (spherical diameter 2.67 mm). The contact angles were measured using a commercial goniometer (OCAH200, Dataphysics). For flat OTS coated surfaces, the contact angle was measured to be $\theta = 105^\circ \pm 1^\circ$. The measured contact angles for these structured surfaces are plotted as solid symbols in the graph shown in Figure 2; they progressively diverge from the values predicted by the Cassie-Baxter relation (the horizontal dashed lines) as the pillar sizes shrink. The red and blue solid lines are the least-square fits of the

measured values to the relation given by (2) with the single unknown parameter l_{cr} . The relationship's excellent fit to the data with the single fit parameter $l_{cr} = 0.29 \mu\text{m}$ across all the scales confirms that, compared to the Cassie-Baxter relationship, the new model captures important physical effects of great consequence at small scales. To test the extreme case $S \approx l_{cr}$, additional samples were fabricated using photolithography. The obtained pillar structures have S values ranging from 0.23 to 0.40 μm , but there are irregular cross-sections due to the fabricated sizes being close to the photolithography limit (see Appendix). The solid triangle symbols in Figure 2 show the measured contact angles, which are all larger than 170° . The different roughness shapes and area fractions used in these experiments and the measured very high apparent contact angles further confirm the validity of (2) and its ability to predict contact angles when the surface features are in the micron-submicron range.

To exclude the possibility that the increased contact angles arose as a result of finer surface roughness on the pillar tops, perhaps as a result of the photolithography, we examined these using an atomic force microscope. They were observed to be as smooth (with fluctuations on the scale of several Angstroms, see Appendix) as the un-etched silicon wafers, thus confirming that this was not the cause of the large contact angles at small scales seen in the experiments.

The experimental observations in Figure 2 show the tendency of θ^* to approach 180° as S trends downwards toward

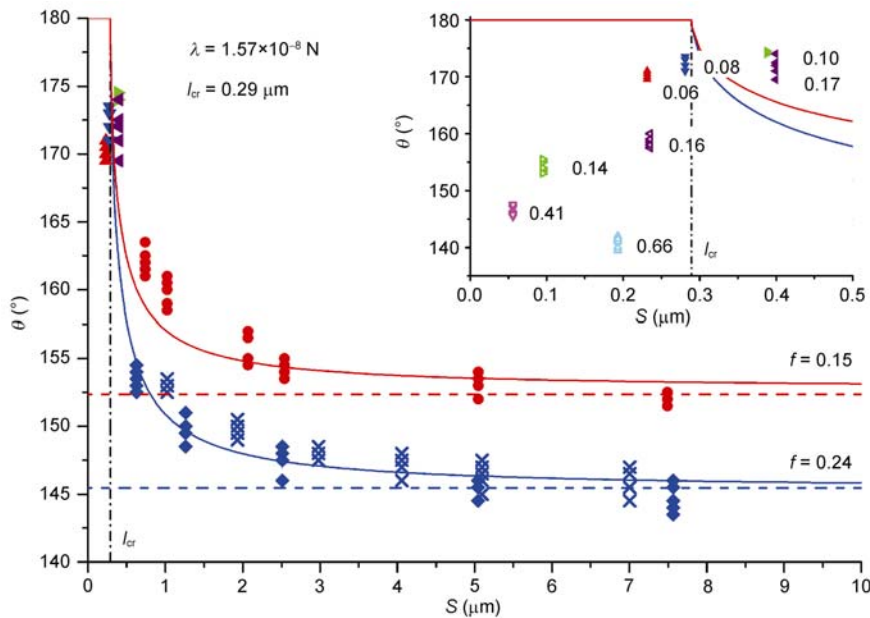


Figure 2 The roughness size dependence of measured contact angles (solid dots) and the least-square fitted curves (solid lines) based on the new relation (2). The data are classified into three sets according to the approximately same area fractions and shapes: red circles and blue diamond solid dots for $f \approx 0.15$ and $f \approx 0.24$ with square-shaped cross-section, and blue crosses for $f \approx 0.24$ with X-shaped ones. The horizontal dashed lines in red and blue give the respective Cassie-Baxter predictions. The fitted value of l_{cr} for all 17 studied samples in the above three sets is equal to $0.29 \mu\text{m}$. The triangle symbols are for four samples with S near l_{cr} . The insert shows the measured contact angles, with their respective area fractions, for eight pillar-structured samples with S near or smaller than l_{cr} .

l_{cr} . Also apparent from the figure is how well the new relation (2) predicts the contact angle. As S further decreases across the critical value, l_{cr} , the relation for the energy release (E) reveals that E resulted from the attachment passing through a transition from positive to negative. Negative E means that attaching water drops onto such rough substrates would be energetically unfavorable compared to their free state in air. As a consequence, the contact angles with $S \leq l_{cr}$ would always take the extreme value of 180° , regardless of the area fraction. To test this, we fabricated four square- or X-shaped pillar-structured samples (Figure 3(a)) with S ranging from 0.06 to $0.24 \mu\text{m}$ using an E-beam technique and made it hydrophobic again by grafting an OTS. The measured values of θ^* are plotted as solid symbols in the insert of Figure 2. Surprisingly, the contact angles for samples with relatively high area fractions are significantly lower than 180° . A possible explanation for this observation may come from the existence of “long-range” hydrophobic interactions that can pull a hung water drop at a distance from tens to hundreds of nanometers to suddenly adhere to the substrate [15–17]. These “long-range” interaction forces come into effect for pillar structures with pillar separations within the submicron range, and make ideal contact angles of 180° impossible. To explain this point, we note that the separation between the water surface and the top of an adjacent pillar to the contacted one is $\Delta \approx b \sin \theta^* + (b^2/2R)(1 + \sin^2 \theta^*)$, where R is the drop radius (Figure 3(b)). For example, for a fabricated sample with $b = 177 \text{ nm}$, $f = 0.66$ and $S = 0.193 \mu\text{m}$ (Insert of Figure 2 and Appendix), Δ will be less than the hydrophobic interaction range l_{int} , say 100 nm , unless $\theta^* < 146^\circ$. On the other hand, to achieve the extremum contact angle $\theta^* \approx 180^\circ$, for a water droplet of $10 \mu\text{L}$ (1.33 mm in radius) with $l_{int} = 100 \text{ nm}$ requires a very large separation of $b > \sqrt{2Rl_{int}} \approx 11.5 \mu\text{m}$. Therefore, the

existence of a submicron hydrophobic interaction range l_{int} sets a lower bound on S for the validity of the scaled-down superhydrophobic mechanism.

There are over 1200 species of water-walking arthropods (insects and spiders) [7,18–20] that support themselves on their superhydrophobic cuticles. To survive environmental disturbances such as the impact of heavy rain they have to maintain a Cassie-Baxter state. Based on the analysis presented here, it is clear how fine-scale roughness can produce a uniquely well-suited surface that allows arthropods to maintain stable superhydrophobicity. For pillar-structured surfaces, it is known that the maximum water pressure sustainable by the surface to prevent the transition from the Cassie-Baxter to the Wenzel state due to the pillars piercing the water is [4]:

$$p_{\max} = -\frac{f}{1-f} \frac{1}{S} \sigma \cos \theta. \quad (3)$$

This clearly shows the trade off between the impact of the scale of the roughness versus the effect of the wet area fraction. These act in opposition to each other in determining the maximum pressure that can be withstood to maintain the Cassie-Baxter state, which is generally required for water-repellency [7]. On the one hand, reducing f results in superhydrophobic surfaces, but this is accompanied by a reduced capacity to withstand the pressure of the liquid; on the other hand, reducing the scale of the roughness yields not only a larger contact angle but also better superhydrophobicity. The above analyses provide the basis to determine the finest submicron scale of naturally occurring superhydrophobic surfaces. It also reveals how such surfaces remain superhydrophobic even in potentially destructive environments, such as the impact of heavy rain, where the impacting pressures can be 10^5 Pa or greater. Furthermore, it is generally known that higher pillars make the Cassie-

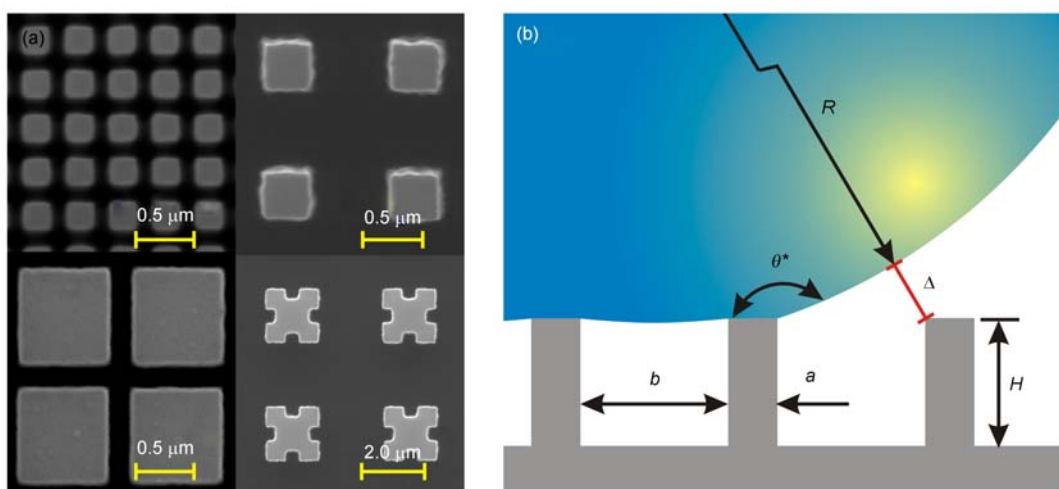


Figure 3 Wetting on pillar-structured surfaces with submicron sizes. (a) SEM images of four samples with S smaller than l_{cr} made from electron beam lithography, and (b) separation Δ between the water surface and the adjacent non-wet pillar top.

Baxter state more stable. The shortest pillar height H that renders the Cassie-Baxter state stable while the Wenzel one is metastable can be obtained by using the same approach as outlined in ref. [4], which gives

$$H_{cr} = \left(l_{cr} + \frac{1-f}{f} S \right) \frac{1 + \cos \theta}{-\cos \theta}. \quad (4)$$

Here, amazingly, the reduction in scale again plays a positive role – lowering the minimum pillar height needed to maintain the Cassie-Baxter state. By contrast, a smaller f pays a higher cost for generating a larger H . Furthermore, increasing H alone makes the pillar structure worse not only from the perspective of bending [7] but also in terms of its susceptibility to the Euler instability [5,6].

The effects of roughness scaling down to some dynamic wetting behaviors were also investigated. We report here two particularly interesting observations. For free falling small water droplets (5.4 μL) released from rest, we observed similar bouncing behavior from our scaled-down generated superhydrophobic surfaces to that from traditional small f generated ones [21]. We show in Figures 4(a) and (b) the observation that both the first bouncing heights and the total number of bounces increase while reducing the roughness scale for the square pillar-structured surfaces with the same area fraction $f \approx 0.15$. Figure 4(c) shows the representative SEM images of pillars from a pillar-structured surface we made with the constant area fraction $f = 0.16$ and gradient pillar sizes. As we vibrate this gradient surface, which is placed horizontally, water drops on the surface move toward the area with larger scales (Figure 4(d)). All these observations can be well explained as consequences of enlarging the contact angle effect by scaling down the roughness

[22], thus giving additional support to the new model (2).

J. Willard Gibbs first articulated the concept of line tension, providing it with a unique thermodynamic conceptual framework. However, there have been ongoing problems with the measurement of line tension. Reported values are unacceptably diverse, with, in some cases [14], order of magnitude differences being reported. This is explained by the small magnitudes of the quantities involved but, as physical effects at small scales come under further scrutiny, the impact of line tension will become increasingly important. To not have accurate values will be embarrassing to say the least. The new relationship presented in this paper (2) can be used to precisely determine line tension of solid-liquid pairs. Without this explanation of experimental observations based on mechanisms involving line tension, this area of research will remain only qualitative. In this regard, previous important observations of the influence of roughness size on contact angles [11–13] were unable to provide the physical understanding given here. Previously proposed models that included the effect of line tension on contact angles for rough substrates only considered line tension effects at the macro-scale in terms of drop dimensions, i.e. at the edges of the droplet’s contact line with the solid surface [23]. Since these models omit the much larger contribution of line energy arising from the apparent contact area, as discussed here, their results do not capture all of the physics involved and so cannot capture the large impact of scale on the wetting angle.

To conclude, scaling down the roughness into the micro-submicron range is a unique and elegant strategy to achieve not only superhydrophobicity, but also to increase its stability against environmental disturbances. Our new model (2) captures important physical effects of great con-

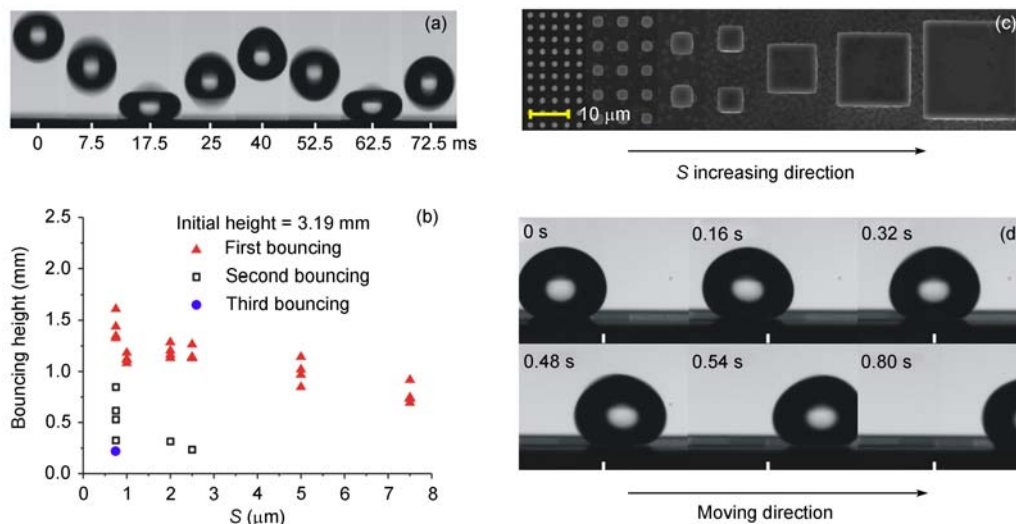


Figure 4 The effects of roughness scaling down with fixed $f \approx 0.15$ on dynamic wetting behavior. (a) Images showing water drops bouncing with time; (b) the bouncing heights versus scale S , the red triangle, blue square and green circle symbols correspond to the first, second and third bounces, respectively; (c) SEM images of the typical pillars on the pillar-structured surface with $f \approx 0.16$ and gradient pillar sizes; (d) selected frames at different times of a video recording of directional horizontal rolling on the horizontally placed gradient surface that vibrates (see Appendix).

sequence at small scales. The above results help us to understand why naturally occurring superhydrophobic surfaces commonly have micron-submicron roughness [7,19,20,24,25] and guide the fabrication of stable super water-repellant surfaces [8,26–32]. As also revealed, the roughness scale is reduced as the maximal contact angle of the roughness scale approaches a fundamental critical length. Further reduction of scale sees the contact angle again drop, probably as a result of entering a new dynamic regime in which new forces play a role. This presents an intriguing insight into nature's selection of optimal resistance to wetting, with further research needed to fully understand the transition across the critical length scale.

Appendix A Sample surfaces and measured contact angles

A1 Sample preparation

A total of 25 superhydrophobic surface samples were fabricated based on silicon wafers with micro-pillars (21 samples) by photolithography and submicro-pillars (four samples) using e-beam lithography which were coated with octadecyltrichlorosilane (OTS, $C_{18}H_{37}Cl_3Si$, 95%).

A3.2 Sizes and contact angles for six square samples designed with $f=0.16$

Table A1 The first set of six surface samples that have the same designed areas $f=0.16$ and pillar heights $H \approx 35 \mu\text{m}$ and their measured geometric parameters and contact angles (CAs) θ^*

No.	Designed				Measured				
	a (μm)	b (μm)	f	S (μm^2)	a (μm)	b (μm)	f	S (μm^2)	θ^*
1	3	4.5	0.16	0.75	2.96	4.54	0.136	0.743	$162.1^\circ \pm 1^\circ$
2	4	6		1	3.94	6.06	0.152	1.025	$159.8^\circ \pm 1^\circ$
3	8	12		2	8.95	11.05	0.156	2.066	$156.0^\circ \pm 1^\circ$
4	10	15		2.5	9.96	15.04	0.158	2.539	$154.3^\circ \pm 1^\circ$
5	20	30		5	19.97	30.03	0.159	5.047	$153.1^\circ \pm 1^\circ$
6	30	45		7.5	29.97	45.03	0.160	7.493	$152.0^\circ \pm 1^\circ$

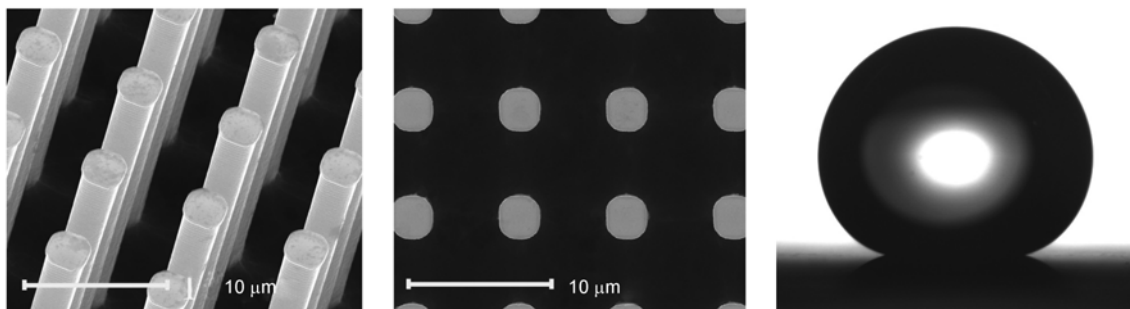


Figure A2 SEM images of Sample No.1 in Table A1 and the droplet with measured $\theta^*=162.1^\circ \pm 1^\circ$.

A2 Contact angle measurement

The droplets were deionized water, and their volumes were fixed to be $10 \mu\text{L}$. The experiments were carried out at room temperature. The contact angles (CAs) were measured by using a goniometer (OCAH200, Dataphysics, Germany).

A3 Summary of results

The dimensions and SEM (FEI, Quanta 200F) image of each of these samples and the typical observed water droplets and measured contact angles are summarized below.

A3.1 Intrinsic contact angle θ

The intrinsic contact angle measured on a flat surface with the OTS coating is $105^\circ \pm 1^\circ$, as illustrated in Figure A1.

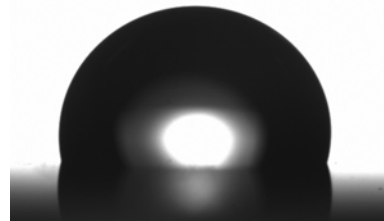


Figure A1 A droplet on a flat surface, with the measured contact angle = $105^\circ \pm 1^\circ$.

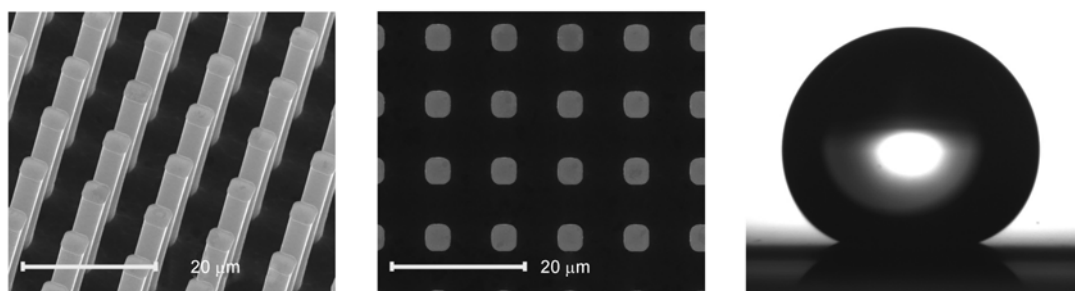


Figure A3 SEM images of Sample No.2 in Table A1 and the droplet with measured $\theta^*=159.8^\circ\pm 1^\circ$.

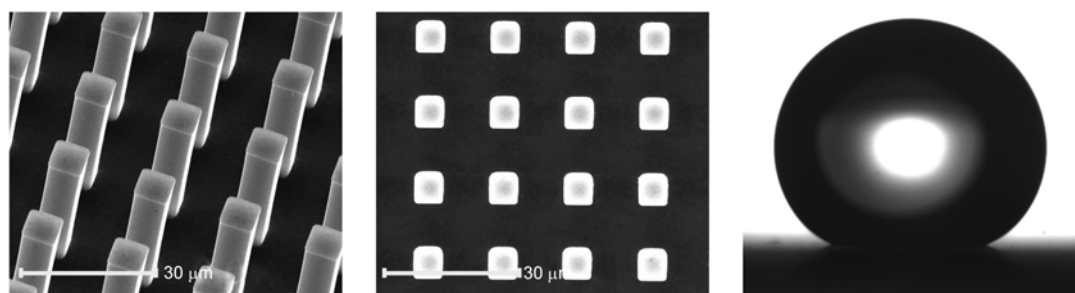


Figure A4 SEM images of Sample No.3 in Table A1 and the droplet with measured $\theta^*=156.0^\circ\pm 1^\circ$.

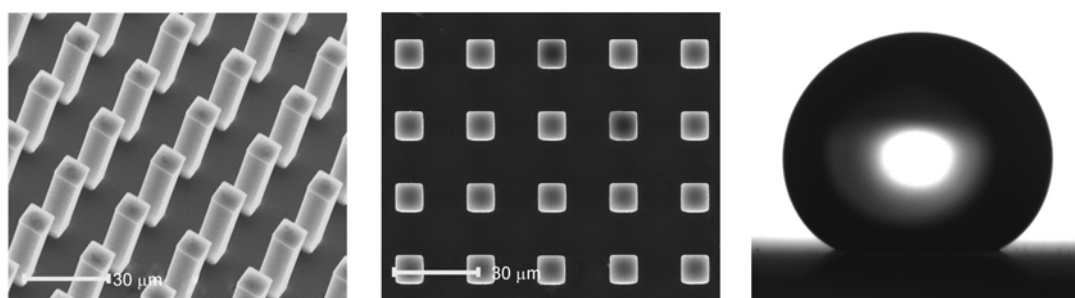


Figure A5 SEM images of Sample No.4 in Table A1 and the droplet with measured $\theta^*=154.3^\circ\pm 1^\circ$.

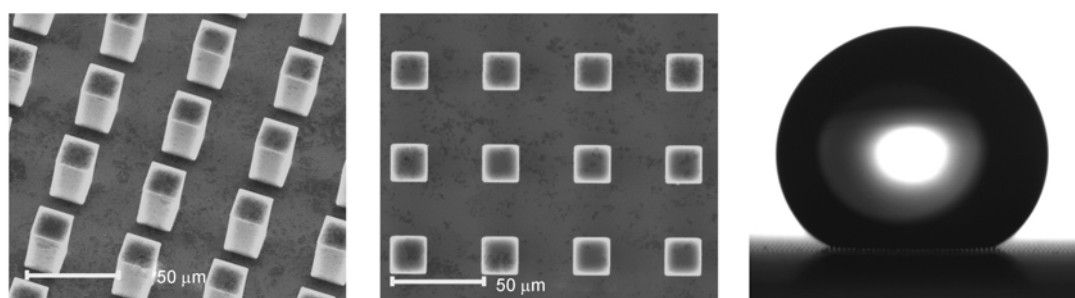


Figure A6 SEM images of Sample No.5 in Table A1 and the droplet with measured $\theta^*=153.1^\circ\pm 1^\circ$.

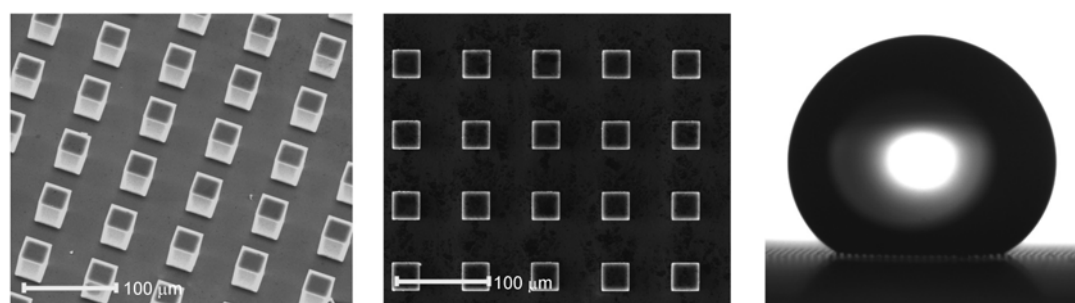
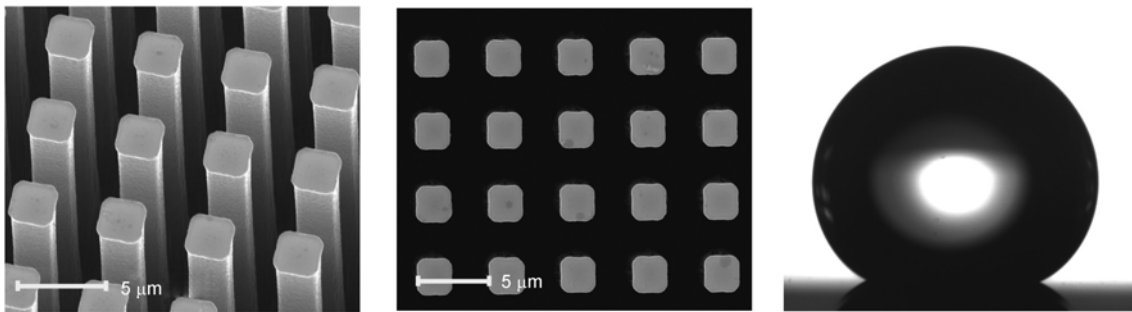
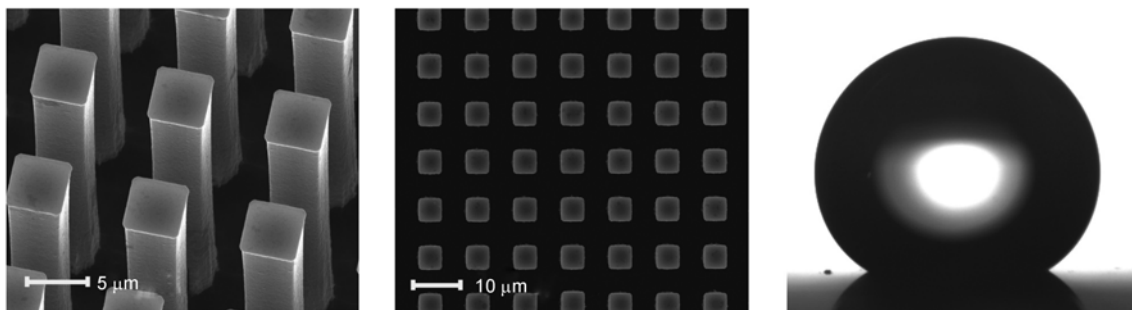
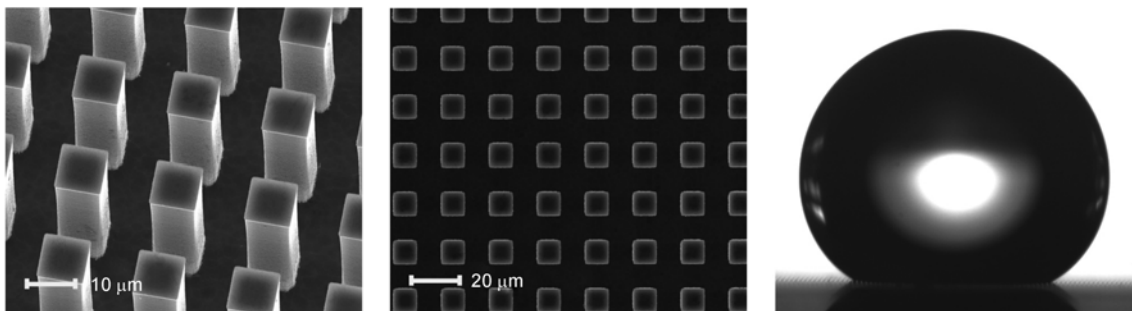


Figure A7 SEM images of Sample No.6 in Table A1 and the droplet with measured $\theta^*=152.0^\circ\pm 1^\circ$.

A3.3 Sizes and contact angles for five square samples designed with $f=0.25$ **Table A2** The second set of five surface samples that have the same designed areas $f=0.25$ and pillar heights $H \approx 35 \mu\text{m}$ and their measured geometric parameters and contact angles (CAs) θ^*

No	Original design				Measured				
	a (μm)	b (μm)	f	S (μm)	a (μm)	b (μm)	f	S (μm)	θ^*
7	2.5	2.5		0.625	2.49	2.51	0.232	0.629	$153.5^\circ \pm 1^\circ$
8	5	5		1.25	4.91	5.09	0.238	1.262	$149.8^\circ \pm 1^\circ$
9	10	10	0.25	2.5	9.96	10.04	0.248	2.512	$147.6^\circ \pm 1^\circ$
10	20	20		5	20.05	19.95	0.251	5.045	$145.6^\circ \pm 1^\circ$
11	30	30		7.5	30.08	29.92	0.251	7.566	$144.7^\circ \pm 1^\circ$

**Figure A8** SEM images of Sample No.7 in Table A2 and the droplet with measured $\theta^*=153.5^\circ \pm 1^\circ$.**Figure A9** SEM images of Sample No.8 in Table A2 and the droplet with measured $\theta^*=149.8^\circ \pm 1^\circ$.**Figure A10** SEM images of Sample No.9 in Table A2 and the droplet with measured $\theta^*=147.6^\circ \pm 1^\circ$.

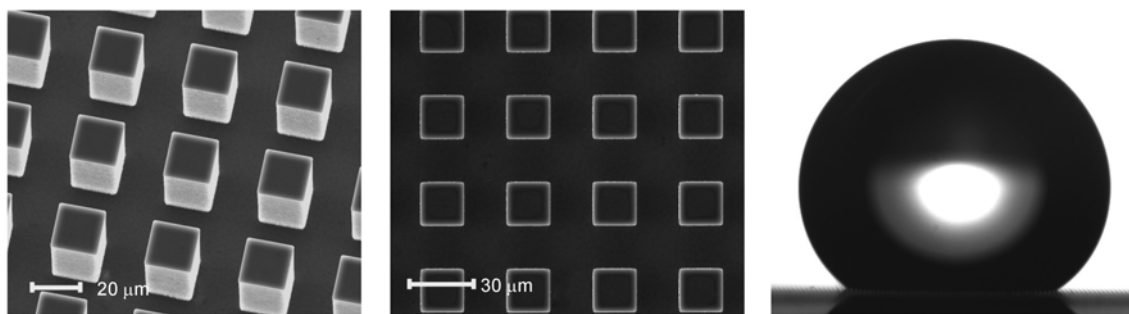


Figure A11 SEM images of Sample No.10 in Table A2 and the droplet with measured $\theta^*=145.6^\circ\pm 1^\circ$.

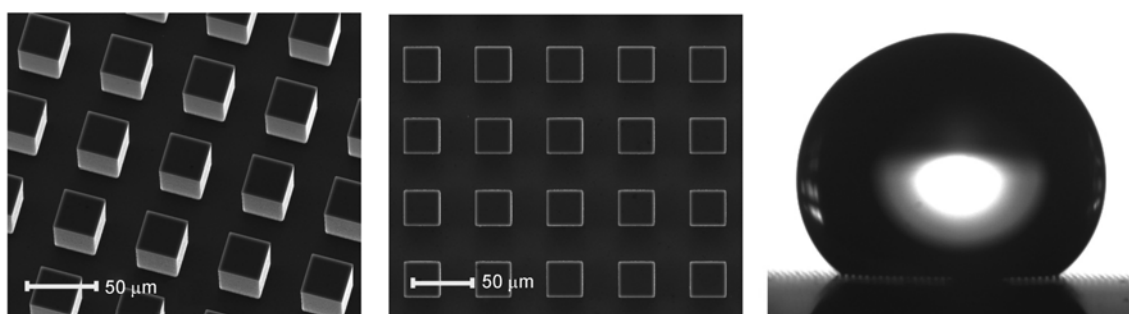


Figure A12 SEM images of Sample No.11 in Table A2 and the droplet with measured $\theta^*=144.7^\circ\pm 1^\circ$.

A3.4 Sizes and contact angles for six X-shaped samples designed with $f=0.245$

Table A3 The third set of six surface samples that have the same designed areas $f=0.245$ and pillar heights $H \approx 35 \mu\text{m}$ and their measured geometric parameters and contact angles (CAs) θ^*

No	Original design				Measured				
	a (μm)	b (μm)	f	S (μm^2)	a (μm)	b (μm)	f	S (μm^2)	θ^*
12	8	6	0.245	1	7.412	6.588	0.191	1.024	$153.1^\circ\pm 1^\circ$
13	16	12		2	15.409	12.591	0.207	1.932	$149.8^\circ\pm 1^\circ$
14	24	18		3	23.532	18.468	0.225	2.981	$148.0^\circ\pm 1^\circ$
15	32	24		4	31.567	24.433	0.231	4.058	$147.2^\circ\pm 1^\circ$
16	40	30		5	39.708	30.292	0.234	5.094	$146.4^\circ\pm 1^\circ$
17	48	42		7	55.718	42.282	0.236	7.007	$145.8^\circ\pm 1^\circ$

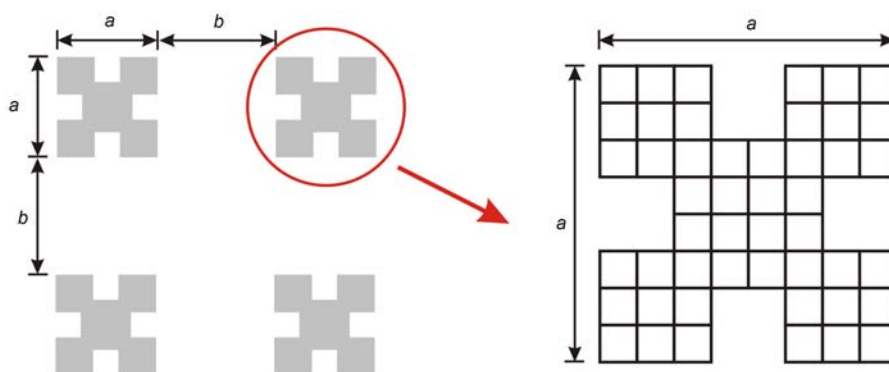


Figure A13 View of the designed geometrical parameters of the X-shaped micro-pillars.

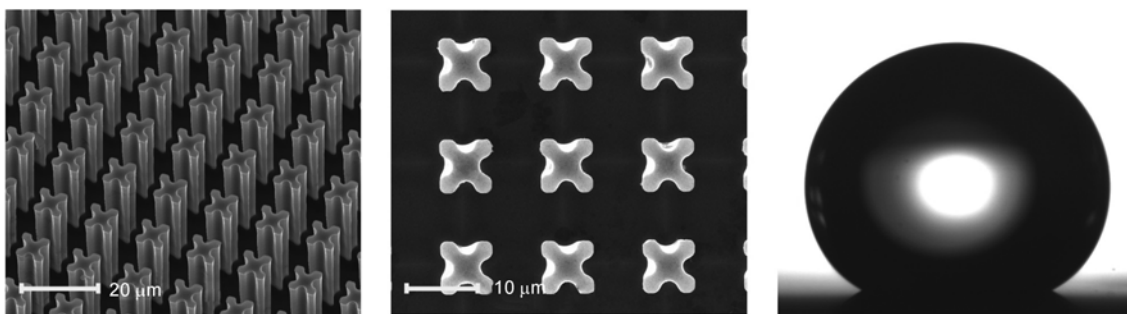


Figure A14 SEM images of Sample No.12 in Table A3 and the droplet with measured $\theta^*=153.1^\circ\pm 1^\circ$.

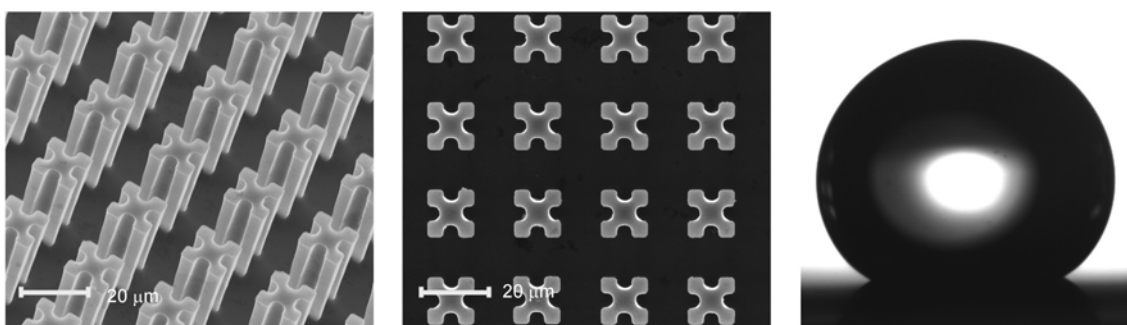


Figure A15 SEM images of Sample No.13 in Table A3 and the droplet with measured $\theta^*=149.8^\circ\pm 1^\circ$.

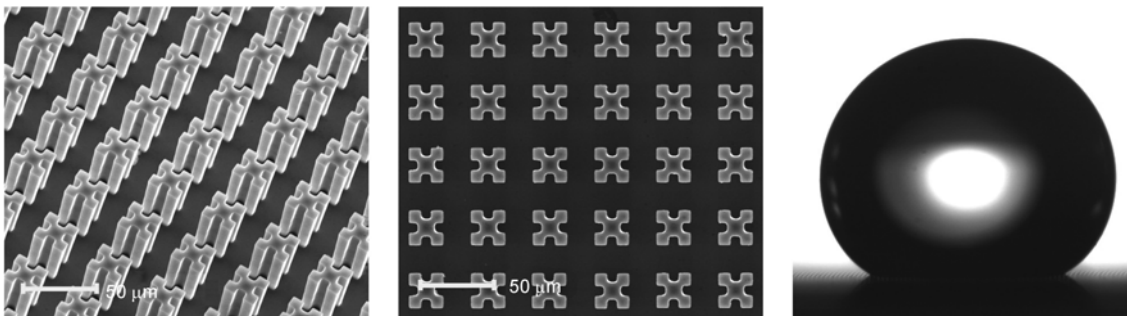


Figure A16 SEM images of Sample No.14 in Table A3 and the droplet with measured $\theta^*=148.0^\circ\pm 1^\circ$.

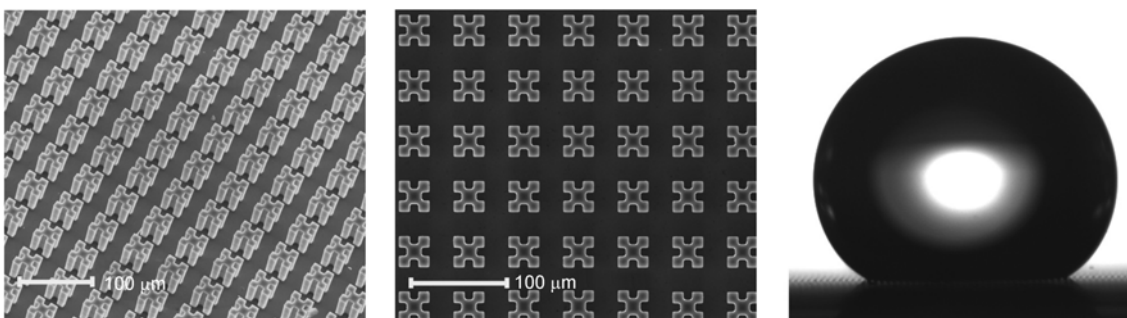


Figure A17 SEM images of Sample No.15 in Table A3 and the droplet with measured $\theta^*=147.2^\circ\pm 1^\circ$.

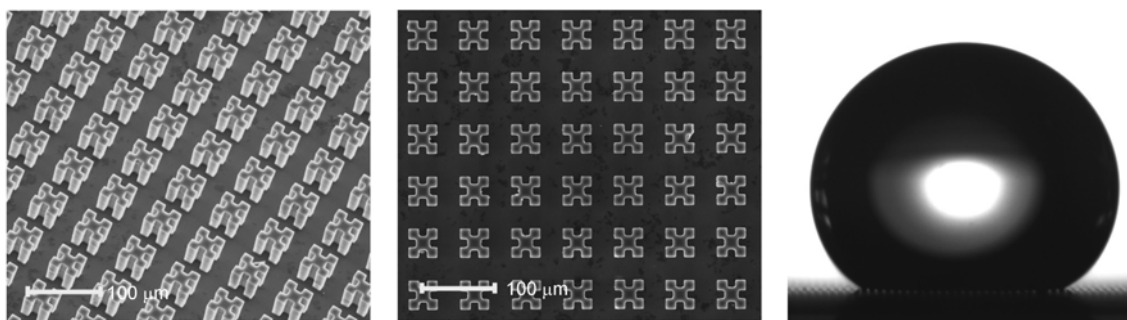


Figure A18 SEM images of Sample No.16 in Table A3 and the droplet with measured $\theta^*=146.4^\circ\pm 1^\circ$.

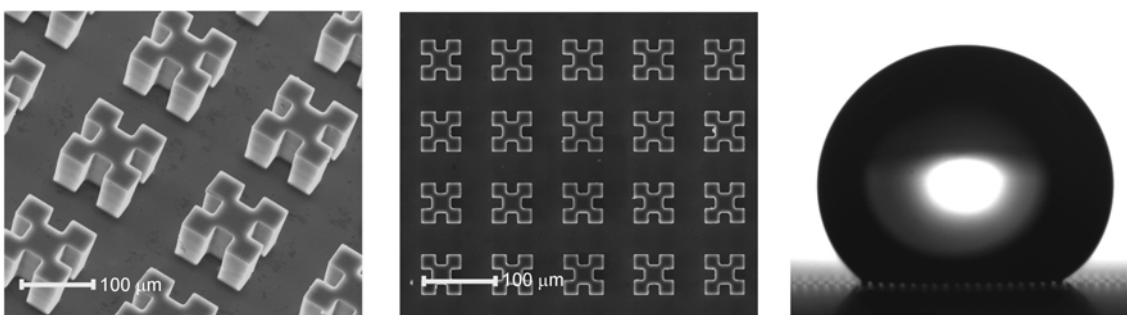


Figure A19 SEM images of Sample No.17 in Table A3 and the droplet with measured $\theta^*=145.8^\circ\pm 1^\circ$.

A3.5 Sizes, shapes and contact angles for four finer samples with S near the critical length l_{cr}

Table A4 The fourth set of four surface samples with pillar heights $H \approx 8 \mu\text{m}$ and their measured geometric parameters and contact angles θ^*

No.	Measured		
	f	$S (\mu\text{m})$	θ^*
18	0.079	0.281	$172.3^\circ\pm 1^\circ$
19	0.171	0.388	$174.1^\circ\pm 1^\circ$
20	0.102	0.399	$171.8^\circ\pm 1^\circ$
21	0.061	0.231	$170.2^\circ\pm 1^\circ$

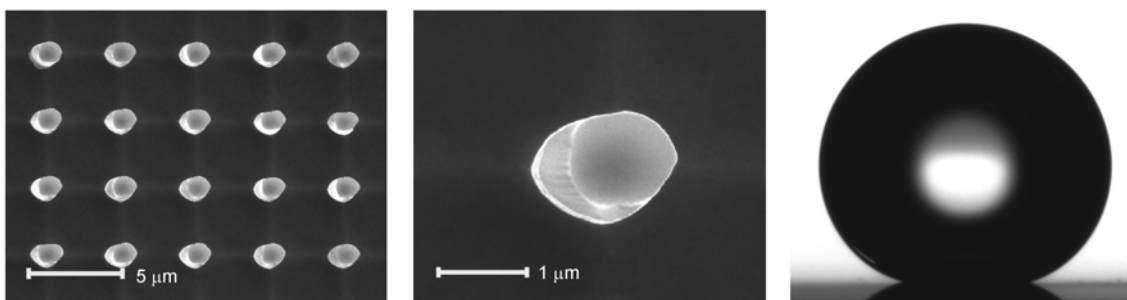


Figure A20 SEM images of Sample No.18 in Table A4 and the droplet with measured $\theta^*=172.3^\circ\pm 1^\circ$.

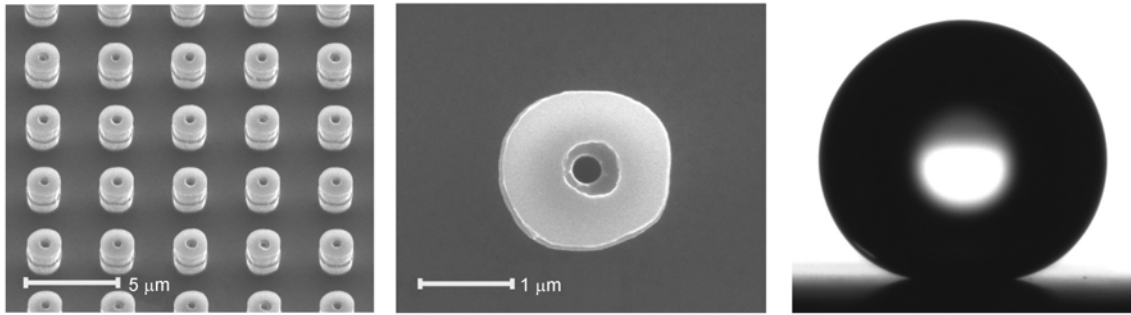


Figure A21 SEM images of Sample No.19 in Table A4 and the droplet with measured $\theta^* = 174.1^\circ \pm 1^\circ$.

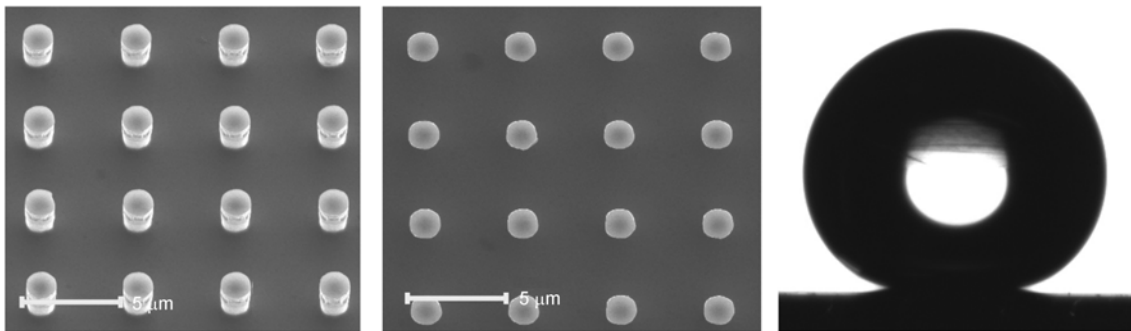


Figure A22 SEM images of Sample No.20 in Table A4 and the droplet with measured $\theta^* = 171.8^\circ \pm 1^\circ$.

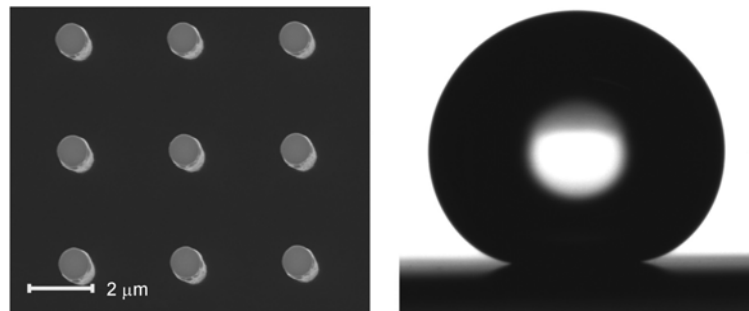


Figure A23 SEM images of Sample No.21 in Table A4 and the droplet with measured $\theta^* = 170.2^\circ \pm 1^\circ$.

A3.6 Sizes, shapes and contact angles for four e-beam fabricated samples with S smaller than the critical length l_{cr}

Table A5 The samples with pillar heights $H \approx 1 \mu\text{m}$ and their measured geometric parameters and contact angles θ^*

No.	Original design				Measured				
	a (μm)	b (μm)	f	S (μm)	a (μm)	b (μm)	f	S (μm)	θ^*
22	0.250	0.100	0.510	0.063	0.224	0.126	0.410	0.056	$146.4^\circ \pm 1^\circ$
23	0.750	0.200	0.623	0.188	0.773	0.177	0.662	0.193	$140.8^\circ \pm 1^\circ$
24	0.4	0.6	0.16	0.1	0.385	0.615	0.141	0.095	$154.2^\circ \pm 1^\circ$

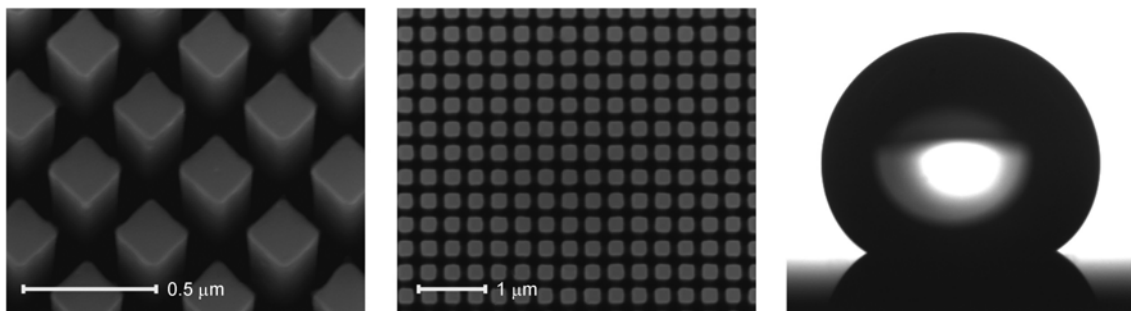


Figure A24 SEM images of Sample No.22 in Table A5 and the droplet with measured $\theta^*=146.4^\circ\pm 1^\circ$.

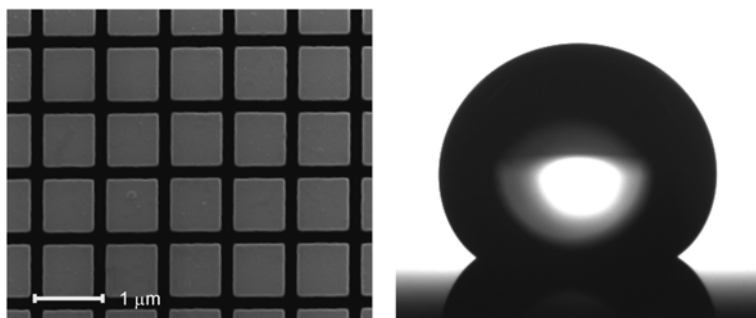


Figure A25 SEM images of Sample No.23 in Table A5 and the droplet with measured $\theta^*=140.8^\circ\pm 1^\circ$.

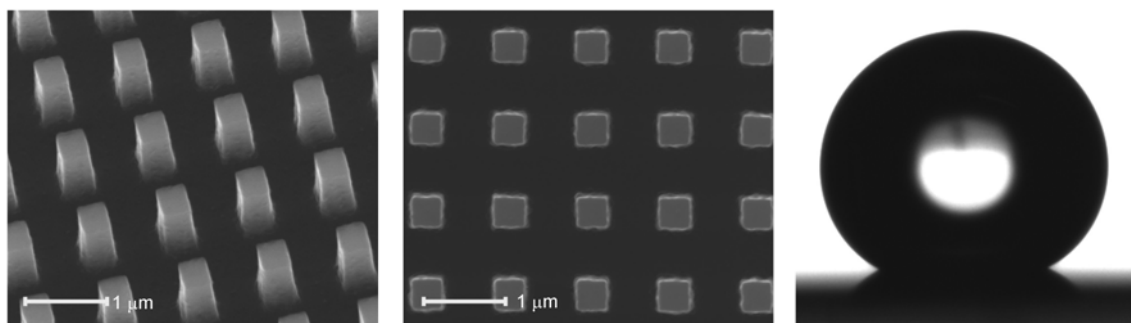


Figure A26 SEM images of Sample No.24 in Table A5 and the droplet with measured $\theta^*=154.2^\circ\pm 1^\circ$.

Table A6 The samples with pillar heights $H \approx 1 \mu\text{m}$ and their measured geometric parameters and contact angles (CAs) θ^*

No.	Original design				Measured				θ^*
	$a (\mu\text{m})$	$b (\mu\text{m})$	f	$S (\mu\text{m})$	$a (\mu\text{m})$	$b (\mu\text{m})$	f	$S (\mu\text{m})$	
25	1.6	1.870	0.16	0.2	1.584	1.886	0.162	0.235	$158.6^\circ\pm 1^\circ$

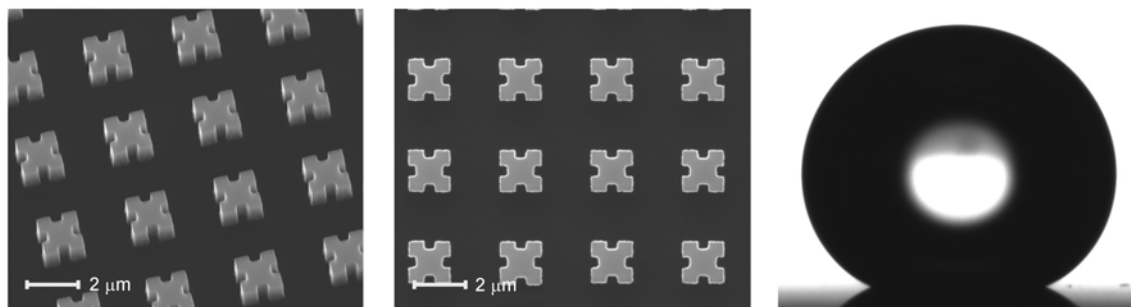


Figure A27 SEM images of Sample No.25 in Table A6 and the droplet with measured $\theta^*=158.6^\circ\pm 1^\circ$.

A3.7 The smoothness of the top surfaces of pillars

To exclude the possibility that the increased contact angles arose as a result of finer surface roughness on the pillar tops, we examined these using an atomic force microscope. They were observed to be as smooth (with fluctuations on the scale of several Angstroms, Figure S28) as the un-etched silicon wafer, thus confirming that this was not the cause of the large contact angles at small scales seen in the experiments.

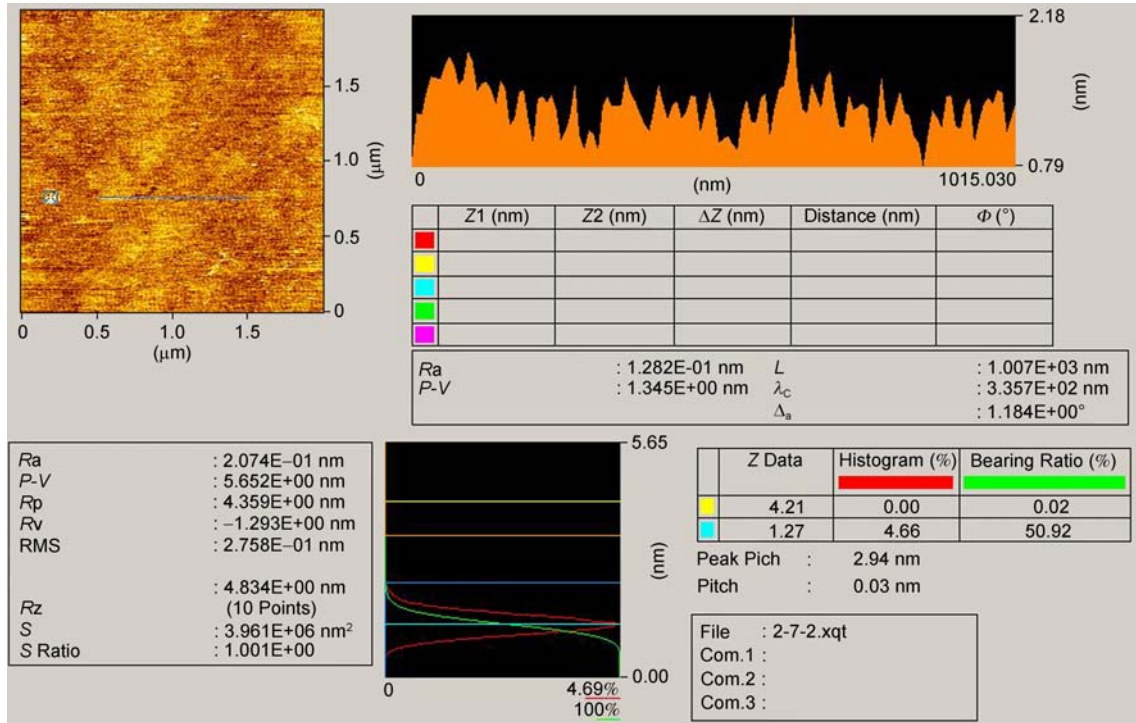


Figure A28 AFM (SPA-400) of the micro-substrates; the pictures were obtained from the top of one of the micro-pillars, Ra=2.074 Å, RMS=2.758 Å.

Appendix B Gradient micro-structured substrates

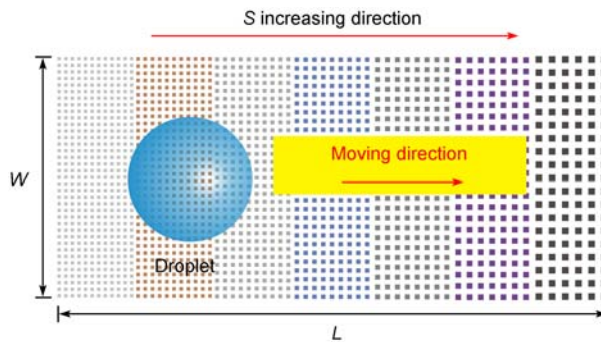


Figure B1 Illustrative sketch of the designed gradient structured substrate; the total length L of the seven-area sample is 1.4 cm and the width W is 0.8 cm.

Table B1 Geometric parameters of the micro-pillars in the gradient structured substrates

No.	Original design				Measured			
	a (μm)	b (μm)	f	S (μm)	a (μm)	b (μm)	f	S (μm)
1	2	3		0.5	1.97	3.05	0.154	0.493
2	4	6		1	3.92	6.14	0.152	0.980
3	6	9		1.5	5.97	9.10	0.157	1.493
4	10	15	0.16	2.5	9.93	15.29	0.155	2.483
5	20	30		5	20.20	29.87	0.163	5.050
6	30	45		7.5	30.25	45.04	0.161	7.563
7	40	60		10	40.12	60.03	0.161	10.030

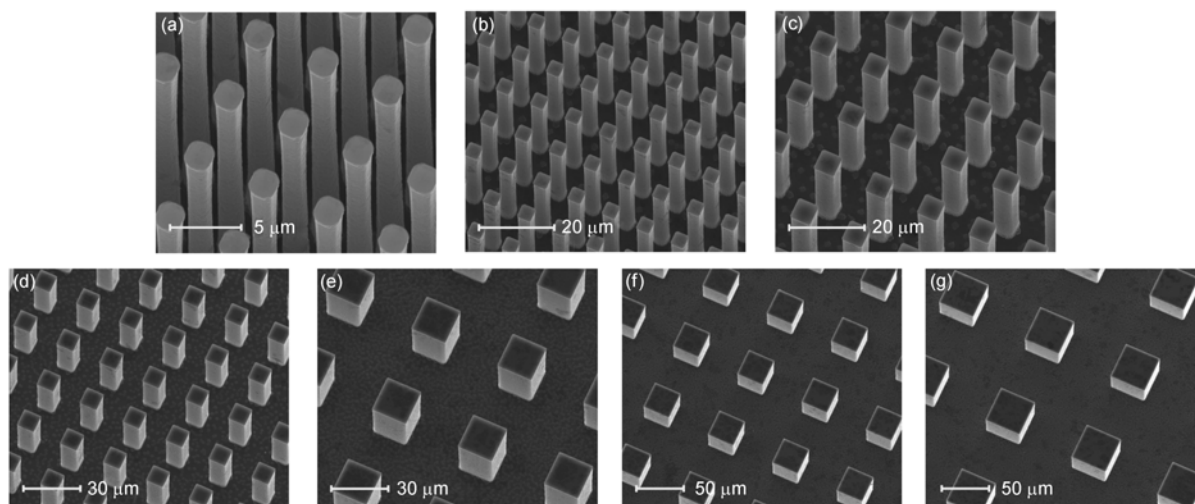


Figure B2 SEM images of the gradient structured substrate; (a)–(g) correspond to Figure B1 and Table B1 respectively.

We thank Profs. LI XiDe, YIN YaJin, and LI QunQing for helpful discussions and sample preparation. Financial support from the National Natural Science Foundation of China (Grant Nos. 10672089, 10772100, 10832005, and 11072126) and from the National Basic Research Program of China (Grant No. 2007CB936803) is gratefully acknowledged.

- Wenzel R N. Resistance of solid surfaces to wetting by water. *Ind Eng Chem*, 1936, 28: 988–994
- Cassie A B D, Baxter S. Wettability of porous surfaces. *Trans Faraday Soc*, 1944, 40: 546–551
- Lafuma A, Quéré D. Superhydrophobic states. *Nat Mater*, 2003, 2: 457–460
- Zheng Q S, Yu Y, Zhao Z H. Effects of hydraulic pressure on the stability and transition of wetting modes of superhydrophobic surfaces. *Langmuir*, 2005, 21: 12207–12212
- Yu Y, Zhao Z H, Zheng Q S. Mechanical and superhydrophobic stabilities of two-scale surficial structure of lotus leaves. *Langmuir*, 2007, 23: 8212–8216
- Lobato E J, Salamon T R. Computation of constant mean curvature surfaces: Application to the gas-liquid interface of a pressurized fluid on a superhydrophobic surface. *J Colloid Interface Sci*, 2007, 314: 184–198
- Bush J W M, Hu D L, Prakash M. The integument of water-walking arthropods: Form and function. *Adv Insect Physiol*, 2008, 34: 117–192
- Blossey R. Self-cleaning surfaces-Virtual realities. *Nat Mater*, 2003, 2: 301–306
- Shafirin E G, Zisman W A. In *Contact Angle, Wettability and Adhesion*. Advances in Chemistry series. In: Fowkes F M, ed. Washington D C: American Chemical Society, 1964. 43: 145–167
- Bico J, Marzolin C, Quéré D. Pearl drops. *Europhys Lett*, 1999, 47: 220–226
- Youngblood J P, McCarthy T J. Ultrahydrophobic polymer surfaces prepared by simultaneous ablation of polypropylene and sputtering of poly (tetrafluoroethylene) using radio frequency plasma. *Macromolecules*, 1999, 32: 6800–6806
- Öner D, McCarthy T J. Ultrahydrophobic surfaces. Effects of topography length scales on wettability. *Langmuir*, 2000, 16: 7777–7782
- Onda T, Shibuchi S, Satoh N, et al. Super-water-repellent fractal surfaces. *Langmuir*, 1996, 12: 2125–2127
- Amirfazli A, Neumann A W. Status of the three-phase line tension. *Adv Colloid Interface Sci*, 2004, 110: 121–141
- Christenson H K, Claesson P M. Cavitation and the interaction between macroscopic hydrophobic surfaces. *Science*, 1988, 239: 390–392
- Carambassis A, Jonker L C, Attard P, et al. Force measured between hydrophobic surfaces due to a submicroscopic bridging bubble. *Phys Rev Lett*, 1998, 80: 5357–5360
- Singh S, Houston J, Swol F, et al. Drying transition of confined water. *Nature*, 2006, 442: 526
- Andersen N M. *The Semiaquatic Bugs (Hemiptera, Gerromorphs): Phylogeny, Adaptations, Biogeography and Classification*. Klampenborg, Denmark: Scandinavian Science Press Ltd., 1982
- Gao X F, Jiang L. Water-repellent legs of water strider. *Nature*, 2004, 432: 36
- Hu D L, Bush J W M. Meniscus-climbing inserts. *Nature*, 2005, 437: 733–736
- Jung Y C, Bhushan B. Dynamic effects of bouncing water droplets on superhydrophobic surfaces. *Langmuir*, 2008, 24: 6262–6269
- Richard D, Clanet C, Quéré D. Contact time of a bouncing drop. *Nature*, 2002, 417: 811
- Drelich J, Miller D J. Modification of the Cassie equation. *Langmuir*, 1993, 9: 619–621
- Barthlott W, Neinhuis C. Purity of the sacred lotus, or escape from contamination in biological surfaces. *Planta*, 1997, 202: 1–8
- Parker A R, Lawrence C R. Water capture by a desert beetle. *Nature*, 2001, 414: 33–34
- Tuteja A, Choi W, Ma M, et al. Designing superhydrophobic surfaces. *Science*, 2007, 318: 1618–1622
- Erbil H Y, Demirel A L, Avci Y, et al. Transformation of a simple plastic into a superhydrophobic surface. *Science*, 2003, 299: 1377–1380
- Nealey P F, Black A J, Wilbur J L, Whitesides G M. *Molecular electronics*. Oxford: Blackwell Science, 1997
- Aussillous P, Quéré D. Liquid marbles. *Nature*, 2001, 411: 924–927
- Lahann J, Mitragotri S, Tran T-N, et al. A reversibly switching surface. *Science*, 2003, 299: 371–374
- Courbin L, Denieul E, Dressaire E, et al. Imbibition by polygonal spreading on microdecorated surfaces. *Nat Mater*, 2007, 6: 661–664
- Sanchez C, Arribart H, Guille M M G. Biomimetism and bioinspiration as tools for the design of innovative materials and systems. *Nat Mater*, 2005, 4: 277–288